

Numerical study of heat transfer characteristics of downward supercritical kerosene flow inside circular tubes^{*}

Jing-zhi ZHANG^{1,2}, Jin-pin LIN^{1,2}, Dan HUANG^{1,2}, Wei LI^{†‡1}

¹Department of Energy Engineering, Zhejiang University, Hangzhou 310027, China

²Department of Energy Engineering, Collaborative Innovation Center of Advanced Aero-engine, Zhejiang University, Hangzhou 310027, China

[†]E-mail: weili96@zju.edu.cn

Received Mar. 28, 2016; Revision accepted July 18, 2016; Crosschecked Jan. 16, 2018

Abstract: The heat transfer characteristics of China RP-3 aviation kerosene flowing in a vertical downward tube with an inner diameter of 4 mm under supercritical pressures are numerically studied. A ten-species surrogate model is used to calculate the thermophysical properties of kerosene and the re-normalization group (RNG) k - ε turbulent model with the enhanced wall treatment is adopted to consider the turbulent effect. The effects of mass flow rate, wall heat flux, inlet temperature, and pressure on heat transfer are investigated. The numerical results show that three types of heat transfer deterioration exist for the aviation kerosene flow. The first type of deterioration occurred at the tube inlet region and is caused by the development of the thermal boundary layer, while the other two types are observed when the inner wall temperature or the bulk fuel temperature approaches the pseudo-critical temperature. The heat transfer coefficient increases with the increasing mass flow rate and the decreasing wall heat flux, while the inlet bulk fluid temperature only influences the starting point of the heat transfer coefficient curve plotted against the bulk fluid temperature. The increase of inlet pressure can effectively eliminate the deterioration due to the small variations of properties near the pseudo-critical point at relatively high pressure. The numerical heat transfer coefficients fit well with the empirical correlations, especially at higher pressures (about 5 MPa).

Key words: Aviation kerosene; Heat transfer deterioration; Supercritical pressure; Numerical study

<https://doi.org/10.1631/jzus.A1600276>

CLC number: TK124

1 Introduction

Active regenerative cooling using supercritical hydrocarbon fuels as the primary coolants is one of the most effective and promising technologies to protect the propulsion engine from overheating in aeronautic engineering and advanced gas turbine engine operations (Edwards, 2003). During the process, engine fuels with relatively low temperature are pumped into the cooling channels around the com-

bustion chamber to absorb excess heat prior to entering the engine for combustion, which not only reduces the temperature of the chamber wall but also increases energy release due to fuel preheating. The critical pressure of most hydrocarbon fuels (about 2 MPa) is lower than the typical pressure in the cooling channel for aerospace applications (3–7 MPa). At supercritical pressures, the thermophysical properties of hydrocarbon fuels change dramatically with temperature, and can thus remarkably influence the flow and heat transfer phenomena. When the wall temperature approaches the pseudo-critical temperature, heat transfer enhancement occurs at relatively low heat flux, while heat transfer deterioration can be found at relatively high heat flux. The heat transfer deterioration under certain conditions can even endanger the safety of the system.

[‡] Corresponding author

^{*} Project supported by the National Natural Science Foundation of China (No. 51210011) and the Natural Science Foundation of Zhejiang Province (No. LZ13E060001), China

 ORCID: Wei LI, <https://orcid.org/0000-0002-2295-2542>

© Zhejiang University and Springer-Verlag GmbH Germany, part of Springer Nature 2018

Therefore, further research into the heat transfer characteristics of supercritical hydrocarbon fuels is needed to illustrate underlying physical mechanisms and optimize the engine cooling design.

Many studies have been conducted to investigate the heat transfer performances of supercritical H₂O (Wang et al., 2011; Li Z et al., 2015), CO₂ (Bae and Kim, 2009; Jiang et al., 2013; Yang et al., 2013), and hydrocarbon fuels consisting of small molecules such as methane, *n*-decane, and *n*-heptane. Wang et al. (2010) carried out numerical simulations of the convective heat transfer of low-temperature methane and *n*-heptane inside horizontal mini tubes under supercritical pressures. The results suggest that the local heat transfer deterioration occurs when the wall temperature (T_w) reaches the pseudo-critical temperature (T_{pc}). Pizzarelli et al. (2010) also observed heat transfer deterioration under high wall heat fluxes and concluded that the reduction of turbulent diffusion was the reason for the local heat transfer deterioration. Urbano and Nasuti (2013) numerically investigated the heat transfer deterioration of three light hydrocarbons and found out that a threshold value for the heat flux to mass flow rate ratio existed to trigger the deterioration.

The investigation of aviation kerosene is limited compared to hydrocarbon fuels listed above due to its complicated components and variations of thermophysical properties. The convective heat transfer characteristics of the supercritical kerosene in a horizontal circular tube were numerically investigated by (Dang et al., 2013, 2015) in order to obtain the onset condition of the heat transfer deterioration. They pointed out that the deterioration occurred at the location where T_w approached T_{pc} with the heat flux exceeding a critical value. Turbulent intensity variation caused by drastic changes of thermodynamic and transport properties of kerosene were the main reasons for the deterioration. Huang et al. (2015a, 2015b) experimentally studied the heat transfer characteristics of the upward supercritical kerosene flow inside the vertical tubes and observed heat transfer enhancement and deterioration. The results indicated that the counteracting effects of buoyancy and varied thermophysical properties of kerosene led to the two distinct heat transfer phenomena. Zhang et al. (2012) experimentally studied the heat transfer characteristics of China RP-3 aviation kerosene in vertically

downward mini tubes. The heat transfer deterioration was observed when the ratio between T_w and T_{pc} reached 1.1. Deng et al. (2012) experimentally investigated upward and downward flow and concluded that the heat flux and flow direction influenced the heat transfer characteristics of supercritical aviation fuel. Xu and Meng (2015a, 2015b) paid attention to the surrogate models for calculating thermophysical properties of kerosene and included detailed pyrolytic chemical reaction mechanisms in their simulations.

This study aims to provide further understanding of flow and heat transfer mechanisms of supercritical fluids in downward flow. Heat transfer characteristics of China RP-3 kerosene under supercritical pressures in a vertical tube are numerically investigated. The effects of wall heat flux (q_w), mass flow rate (m), pressure (P), and inlet temperature (T_{in}) on heat transfer are illustrated. Three different kinds of heat transfer deteriorations are discussed in detail. Numerical heat transfer coefficients (HTCs) are compared with empirical correlations to validate the simulation.

2 Numerical approach and validation

In this section, the numerical approach based on the pressure-based solver in FLUENT 15.0 is introduced. The calculation process of thermophysical properties of RP-3 aviation kerosene is presented first followed by the computational configuration and boundary conditions. Lastly, the numerical model is validated by comparing the numerical results with the experimental data.

2.1 Thermophysical properties of kerosene

The thermophysical properties of China RP-3 aviation kerosene were calculated using a ten-species surrogate model proposed by Zhong et al. (2009a) with the extended corresponding states model. A pure hydrocarbon fuel, propane, was adopted as the reference material. The Soave-Redlich-Kwong (SRK) equation of state was employed to calculate the specific heat of kerosene. Details of this model, including the component and mole fraction of the surrogate and detailed calculation process of properties of China RP-3 aviation kerosene, can be found in our previous work (Huang et al., 2015a; Li W et al., 2015).

Fig. 1 shows the variations of properties of RP-3 aviation kerosene with temperatures at 3–5 MPa. Similar to H_2O and CO_2 , aviation kerosene experiences dramatic variation of thermophysical properties near T_{pc} . As shown in Fig. 1, the specific heat reaches a peak value at T_{pc} . Moreover, both the density and viscosity decrease remarkably at T_{pc} . The critical pressure and temperature of RP-3 were reported to be 2.4 MPa and 660 K, respectively (Li et al., 2010, 2011). The pseudo-critical temperature of RP-3 is approximately 672, 705, and 716 K at 3, 4, and 5 MPa, respectively. The physical properties of China RP-3 aviation kerosene were simulated by defining a piecewise-linear function of temperature in FLUENT 15.0.

2.2 Computational configuration and boundary conditions

A vertical tube with an inner diameter (d) of 4 mm is adopted in the present work. Both the wall temperature (T_w) and bulk temperature of the kerosene (T_b) were limited to below 820 K during the simulation because China RP-3 aviation kerosene will

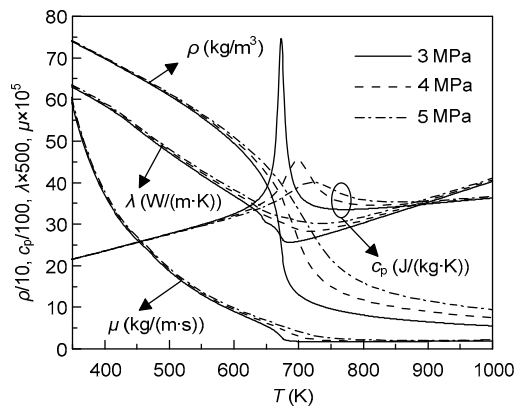


Fig. 1 Variation of the kerosene properties with temperature ($P=3, 4,$ and 5 MPa)

pyrolyze when the fuel temperature reaches approximately 820 K (Zhong et al., 2009b, 2011). To achieve this restriction, the heated length of the tube was chosen carefully from 560 mm to 2100 mm according to different cases.

Fig. 2 shows the sketch of the circular tube with a heated length of 1000 mm. An unheated section of 150 mm was set before the heated section to achieve the fully developed turbulent flow. A 2D computational domain was employed to represent the axisymmetric physical model. A velocity inlet with a constant temperature and a pressure outlet with a constant static pressure were applied at the upstream and downstream boundaries, respectively. A no slip boundary condition was used for the tube wall with a constant heat flux. A zero normal gradient boundary condition was adopted at the symmetry axis for all variables.

As shown in Fig. 2, structured rectangular meshes were adopted in the whole flow region with a fine boundary layer mesh near the wall region. The first grid point adjacent to the wall was constructed to satisfy the requirement of $y^+ \leq 1$ (y^+ is the non-dimensional wall distance, which is defined as $y\sqrt{\tau_w/\rho}/\nu$, where y is the distance to the nearest wall, τ_w is the wall shear stress, ρ is the density, and ν is the kinematic viscosity) and more than 10 grids were placed within the viscosity-affected near-wall region ($Re_y < 200$, where Re_y is defined as $\rho y\sqrt{k}/\mu$, k is the turbulent kinetic energy, and μ is the dynamic viscosity). The mesh sensitivity study was conducted using two grid configurations with radial and axial grid points of 50×2000 and 100×4000 at $m=3.5$ g/s, $P=3$ MPa, $q_w=250$ kW/m², and $T_{in}=423$ K. The maximum relative errors are 0.8% and 2.0% for T_w and HTC, respectively. As a result, 50×2000 was chosen as the final grid configuration.

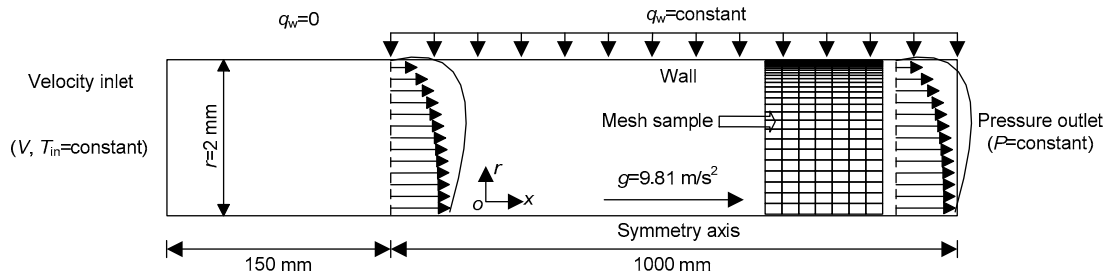


Fig. 2 Schematic of the computational configuration

2.3 Turbulent model

The 2D Reynolds averaged Navier-Stokes (RANS) equations and the energy equation were properly solved by the finite volume method with the pressure-based solver in FLUENT 15.0. The Green-Gauss node-based method was adopted for the evolution of gradients. The semi-implicit method for pressure linked equations-consistent (SIMPLEC) algorithm was employed as the velocity-pressure coupling method and the 2nd-order upwind scheme was chosen to disperse the momentum terms and energy terms. The default values of the under-relaxation factors were adopted to achieve a fast convergence. The convergent residual criteria were set to be 1.0×10^{-6} for mass conservation and turbulent equations and to be 1.0×10^{-8} for momentum and energy conservation equations.

The governing equations are given below:
continuity equation:

$$\frac{\partial}{\partial x_i}(\rho u_i) = 0; \quad (1)$$

momentum equation:

$$\begin{aligned} & \frac{\partial}{\partial x_i}(\rho u_i u_j) \\ &= \frac{\partial}{\partial x_j} \left[\mu_e \left(\frac{\partial u_i}{\partial x_j} + \frac{\partial u_j}{\partial x_i} \right) - \frac{2}{3} \mu_e \frac{\partial u_k}{\partial x_k} \right] - \frac{\partial P}{\partial x_i} + \rho g_i; \end{aligned} \quad (2)$$

energy equation:

$$\begin{aligned} & \frac{\partial}{\partial x_i}(\rho u_i c_p T) \\ &= \frac{\partial}{\partial x_i} \left(k_e \frac{\partial T}{\partial x_i} \right) + \frac{\partial u_i}{\partial x_i} \left[\mu_e \left(\frac{\partial u_i}{\partial x_j} + \frac{\partial u_j}{\partial x_i} \right) - \frac{2}{3} \mu_e \frac{\partial u_k}{\partial x_k} \delta_{ij} \right]. \end{aligned} \quad (3)$$

In Eqs. (1)–(3), ρ is the density (kg/m^3); u is the velocity (m/s); c_p is the specific heat capacity ($\text{J}/(\text{kg}\cdot\text{K})$); T is the temperature (K); x is coordinate value (m); P is the pressure (Pa); g is the gravity (m/s^2); k_e is the ef-

fective thermal conductivity ($\text{W}/(\text{m}\cdot\text{K})$); μ_e is the effective dynamic viscosity ($\text{kg}/(\text{m}\cdot\text{s})$); δ is the unit tensor; the subscripts i, j , and k are indexes of the tensor.

The re-normalization group (RNG) k - ε model with an enhanced wall treatment was adopted to consider the turbulent effect for its wide applications and relatively high accuracy for the flows under supercritical pressures (Li et al., 2010, 2011; Dang et al., 2015). The transport equations for the RNG k - ε model turbulent model are shown as follows (Wang et al., 2015):

$$\frac{\partial}{\partial x_i} \left[\rho k u_i - \left(\mu + \frac{\mu_t}{\sigma_k} \right) \frac{\partial k}{\partial x_i} \right] = P_k + G_k - \rho \varepsilon + \rho D, \quad (4)$$

$$\begin{aligned} & \frac{\partial}{\partial x_i} \left[\rho \varepsilon u_i - \left(\mu + \frac{\mu_t}{\sigma_\varepsilon} \right) \frac{\partial \varepsilon}{\partial x_i} \right] \\ &= (C_{\varepsilon 1} f_1 P_k + C_{\varepsilon 1} C_{\varepsilon 3} G_k - C_{\varepsilon 2} f_2 \rho \varepsilon) \frac{\varepsilon}{k} + \rho E, \end{aligned} \quad (5)$$

where k is the turbulence kinetic energy (m^2/s^2); ε is the rate of dissipation of k (m^2/s^3); σ is the turbulent Prandtl number; μ_t is the turbulent dynamic viscosity ($\text{kg}/(\text{m}\cdot\text{s})$); P_k is the turbulent shear production (W/m^3); D is the additional term; f_1 and f_2 are functions in the dissipation equation; E is the flow energy (W/kg); $C_{\varepsilon 1}$, $C_{\varepsilon 2}$, and $C_{\varepsilon 3}$ are the model constants; G_k represents the generation of turbulence kinetic energy.

More details of the parameters in these equations can be found in the ANSYS FLUENT help files (ANSYS, 2013).

2.4 Validation

The validation of the fluid properties and the numerical methods was performed by comparing the numerical results with the experimental data in (Deng et al., 2012) at $m=2$ g/s, $P=5$ MPa, $T_{\text{in}}=400$ K, and $q_w=107.88, 254.36$, and 348.20 kW/m^2 .

The measuring uncertainty of the tube outer wall temperature is 0.6%, while no information about the inner wall temperature was provided in (Deng et al., 2012). As shown in Fig. 3, the trend of the numerical wall temperatures fits well with the experimental data. A relatively high deviation is observed near the tube inlet, while the maximum deviation between the numerical results and the experimental data are less than 8.0%.

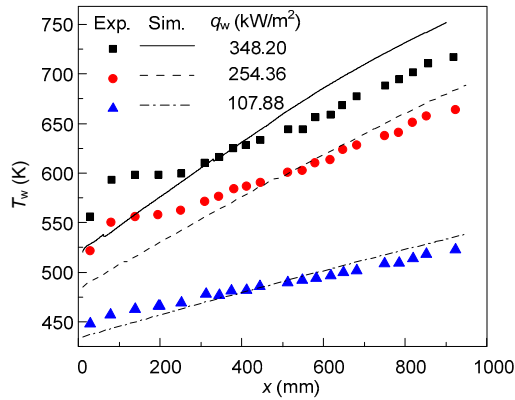


Fig. 3 Comparison between numerical results and experimental data in (Deng et al., 2012)

3 Results and discussion

3.1 Heat transfer deteriorations

Fig. 4 shows the T_w , T_b , and HTC distributions along the tube axial direction at $m=3.5$ g/s, $P=3$ MPa, $q_w=200$ kW/m², and $T_{in}=423$ K. The bulk fuel temperature and heat transfer coefficient are calculated by

$$T_b = \int_A \rho u c_p T dA / \int_A \rho u c_p dA, \quad (6)$$

$$HTC = q_w / (T_w - T_b), \quad (7)$$

where A is the cross-section area (m²); HTC is the heat transfer coefficient (W/(m²·K)); q is the heat flux (kW/m²); the subscripts b and w represent bulk fluid and wall, respectively.

As shown in Fig. 4, T_b and T_w increase gradually along the flow direction, and three types of heat transfer deteriorations exist for the supercritical kerosene flow. Similar deterioration phenomena were also reported in the experimental work by Zhang et al. (2013). T_w shows a drastic increase at the entrance section before the dimensionless distance $x/d=10$, leading to the first type of deterioration (Deterioration near the inlet). In this section, the thermal boundary layer is in the developing stage. The heat transfer recovers after obtaining a minimum heat transfer coefficient at about $x/d=10$, and then T_w increases linearly. When T_w reaches T_{pc} , the second type of deterioration (Deterioration I) is observed, and the increase of T_w becomes steeper. After re-

covering from Deterioration I at about $T_w=1.06T_{pc}$, the third type of deterioration (Deterioration II) is formed between $T_c \leq T_b \leq T_{pc}$.

The second type of deterioration takes place when T_w approaches T_{pc} , and the HTC recovers after obtaining a minimum at $T_w=1.06T_{pc}$. Deterioration I is mainly caused by the drastic changes of aviation kerosene properties and concurrent flow effects such as thermal acceleration when the fluid temperature near the tube wall reaches T_{pc} .

As shown in Fig. 4, the fluid temperature in the near-wall region approaches T_{pc} at the cross-section A, where the heat capacity c_p reaches the maximum value. After that, c_p begins to decrease drastically and strongly reduces the heat transfer ability of the near-wall fluid. Moreover, the decrease of near-wall kerosene density leads to thermal expansion, which increases the specific volume and accelerates the fuel velocity. Though the increased velocity could partially compensate the heat transfer decrease, this effect is overwhelmed by the heat transfer deterioration caused by the decreased c_p and ρ .

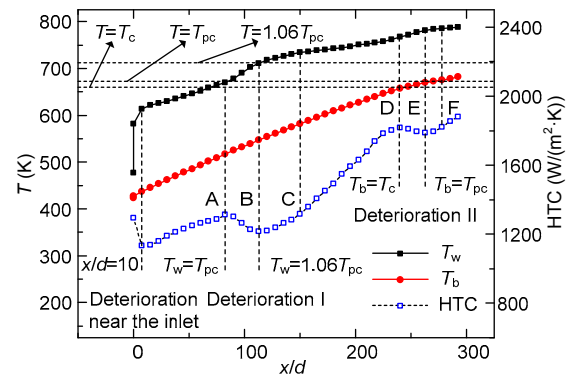


Fig. 4 Wall temperature (T_w), liquid bulk temperature (T_b), and heat transfer coefficient (HTC) distributions along the tube axial direction at $m=3.5$ g/s, $P=3$ MPa, $q_w=200$ kW/m², and $T_{in}=423$ K

The drastic changes of properties near the tube wall also influence the turbulent kinetic energy (k) and the turbulence production term (P_k) distribution along the radial direction. As shown in Fig. 5, k and P_k in the near-wall region both reach the local minimum value at the cross-section B, which means that turbulence in the near-wall region is strongly restrained during Deterioration II. The narrow fluid region with sharp variations of thermophysical properties moves

towards the centerline after the cross-section B, and the turbulence in the near-wall region starts to recover. As a consequence, the HTC increases gradually along the flow direction again before Deterioration II.

$$P_k = \mu_t \left(\frac{\partial \bar{u}}{\partial r} \right)^2 \quad (8)$$

The third type of heat transfer deterioration occurs when T_b approaches around T_c . Unlike Deterioration I, T_w at Deterioration II is much higher than T_{pc} . The re-laminar effect near the tube wall region moves towards the center of the tube. Fig. 6 shows the radial velocity distribution at three cross-sections of D, E, and F. As shown in Fig. 6, the radial velocity from centerline to the near-wall region experiences a sharp decrease and subsequent ascent from the deterioration onset to the heat transfer recovery location. When T_b approaches T_{pc} , the fluid near the wall has a strong trend moving towards the central zone, and thus reduces the mass flow rate in the near-wall region. With a smaller amount of kerosene flowing in

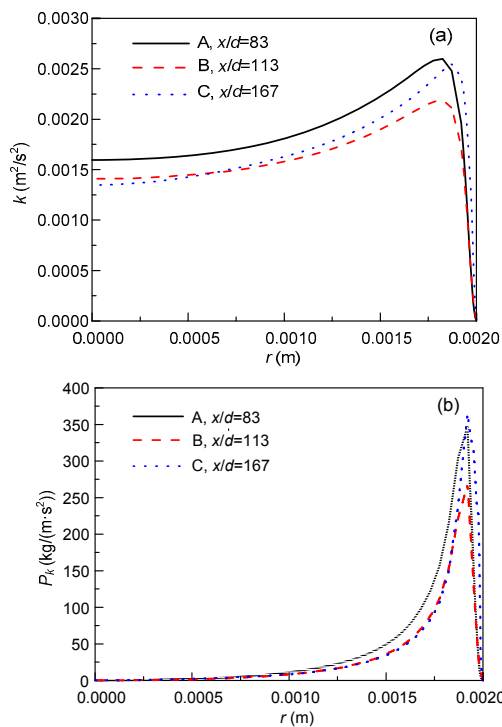


Fig. 5 Distribution of turbulent kinetic energy (a) and turbulence production term (P_k) (b) at different cross-sections of A to C

the near-wall region, the turbulent mixing is reduced, resulting in a decrease in the overall HTC.

Fig. 7 shows the effect of gravity on the heat transfer coefficient. As shown in Fig. 7, T_w under normal gravity is lower than that obtained without gravity, while T_b is independent on the gravity. This leads to a lower HTC for the case under zero-gravity. The gravity shows no effect on the starting point of Deterioration I, but the start of Deterioration II is delayed under zero-gravity. Besides the aforementioned reasons for the deteriorations, the gravity-induced buoyancy also influences the deteriorations for the supercritical flow. However, the gravity effect is also influenced by the mass flux and the tube diameter. More work is needed in the future to study this effect in detail.

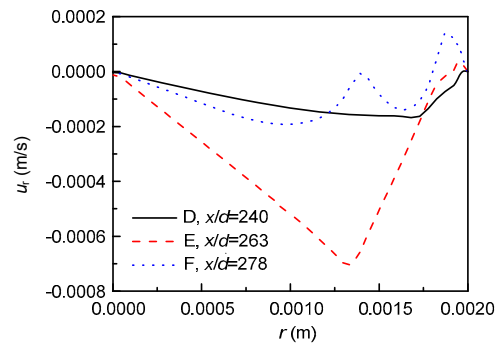


Fig. 6 Distribution of the radial velocity at different cross-sections of D to F

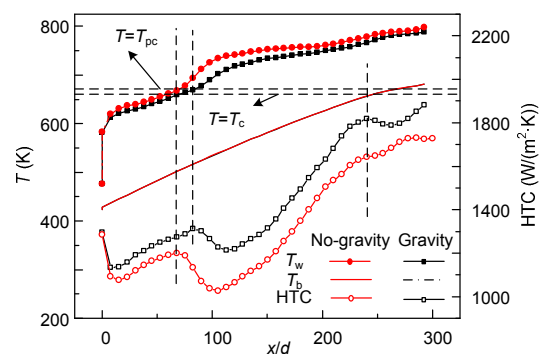


Fig. 7 Gravity effect on T_w , T_b , and HTC at $m=3.5$ g/s, $P=3$ MPa, $q_w=200$ kW/m², and $T_{in}=423$ K

3.2 Influence of the mass flow rate

The effects of the mass flow rate on the heat transfer characteristics of supercritical kerosene inside downward circular tubes were investigated using

four cases with an inlet temperature of 423 K, inlet pressure of 3 MPa, wall heat flux of 200 kW/m², and mass flow rates of 3.0, 3.5, 4.0, and 5.0 g/s. Fig. 8 shows the variations of T_b , T_w , and HTC along the axial direction for the four cases. As shown in Fig. 8, T_b and T_w increase gradually along the flow direction and with a decreasing mass flow rate. The increase of T_w and T_b is slower at a higher mass flow rate due to the higher heat capacity, thus the onset of Deterioration I occurring at $T_w=T_{pc}$ is delayed. The RD, defined in Eq. (9), was used to quantify the relative decreasing proportion of the HTC compared with the onset of the deterioration.

$$RD = \frac{HTC_A - HTC_B}{HTC_A} \quad (9)$$

RD increases from 4.0% at 3.0 g/s to 9.4% at 5.0 g/s, indicating that the smaller growing rates of T_w and T_b at higher mass flow rate lead to a larger heat transfer coefficient deterioration. As shown in Fig. 8b, the length of Deterioration I also increases with an increasing mass flow rate, while the heat transfer coefficient increasing rates between Deterioration I and Deterioration II are the same for the four mass flow rates. Moreover, the T_w after the inlet deterioration increases as the mass flow rate decreases. As a consequence, Deterioration I disappears as the mass flow rate decreases to a relative low value if T_w at the end of the deterioration near the tube inlet is higher than T_{pc} . The onset of Deterioration II also increases with an increasing mass flow rate and even disappears at $m=5$ g/s because T_b at the outlet is still much lower than T_c .

3.3 Influences of the wall heat flux

Four cases with wall heat fluxes of 150, 200, 250, and 300 kW/m² were investigated to study their effects on heat transfer at $m=3.5$ g/s, $P=3$ MPa, and $T_{in}=423$ K. Fig. 9 shows the variations of T_b , T_w , and HTC along the axial direction for the four cases. As shown in Fig. 9, T_w increases sharply at the inlet region, and a much higher T_w is obtained at higher q_w . Although the axial length of the affected region is almost the same, the effect of q_w on the thermal boundary layer is more intense under higher heat flux.

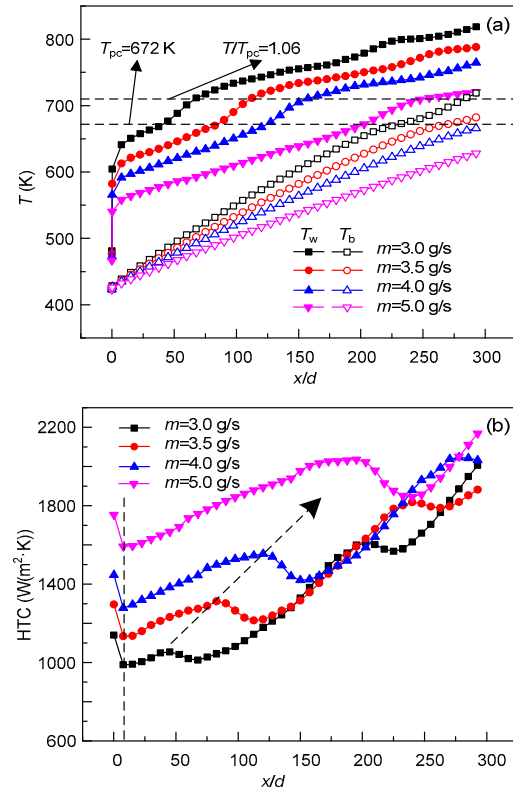


Fig. 8 Distributions of T_w , T_b , and HTC along the tube at $P=3$ MPa, $q_w=200$ kW/m², and $T_{in}=423$ K: (a) variations of T_w and T_b along the tube; (b) variations of HTC along the tube

T_w increases to 775 K after the inlet region at $q_w=300$ kW/m², while the corresponding value is only about 560 K for $q_w=150$ kW/m². As mentioned before, Deterioration I will disappear if T_w , at the end of the deterioration near the tube inlet, is higher than T_{pc} . As shown in Fig. 9, Deterioration I is not observed at $q_w=300$ kW/m² as the onset of Deterioration I falls into the thermal boundary development region. The onsets of Deterioration I and Deterioration II are delayed along the tube axial direction under a lower q_w . Similar conclusions were also reported in the experimental work conducted by Zhang et al. (2012). RD also increases with increasing q_w , indicating that the deterioration is more pronounced at a higher wall heat flux. Under a higher heat flux, T_w increases faster and Deterioration I is restrained within a shorter axial distance. As a consequence, the variation of supercritical kerosene properties in the deterioration region is more drastic, especially for the specific heat

capacity and density. With a rapid decreasing rate of density, the thermal acceleration phenomenon is more obvious, and the turbulent kinetic energy in the near-wall region is suppressed more severely. All these contribute to the more pronounced relative decreasing proportion of the HTC for Deterioration II at a higher wall heat flux.

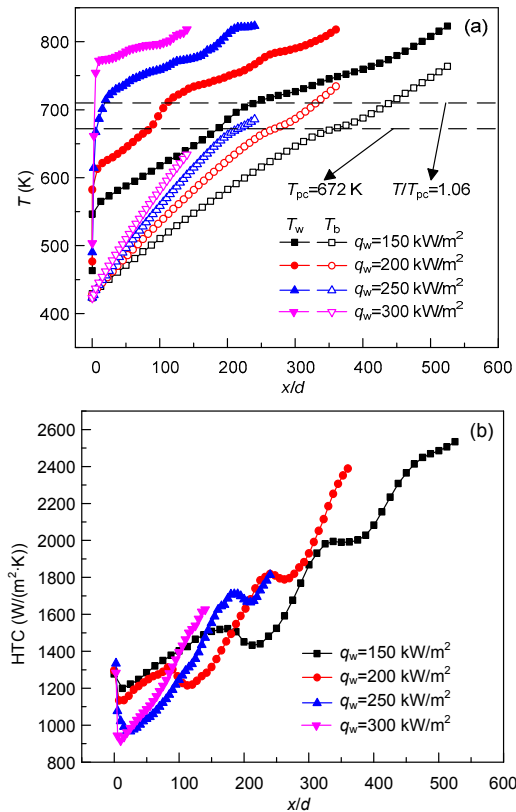


Fig. 9 Distributions of T_w , T_b , and HTC at $m=3.5 \text{ g/s}$, $T_{in}=423 \text{ K}$, and $P=3 \text{ MPa}$ with q_w ranging from 150 kW/m^2 to 300 kW/m^2 : (a) variations of T_w and T_b along the tube; (b) variation of HTC along the tube

3.4 Influences of the inlet temperature

The effect of inlet temperature on the heat transfer characteristics was studied by three cases with different inlet temperatures of 373, 423, and 473 K at $m=3.5 \text{ g/s}$, $P=3 \text{ MPa}$, and $q_w=250 \text{ kW/m}^2$. Fig. 10 depicts the variations of T_b , T_w , and HTC along the axial direction for the three cases. As shown in Figs. 10a and 10b, the onsets of Deterioration I and Deterioration II both move forward along the tube as the inlet temperature rises. T_{in} only affects the starting point of the HTC curve plotted against the bulk flow

temperature. Deterioration I and Deterioration II will disappear if T_{in} is higher than a certain value under a fixed P , q_w , and m .

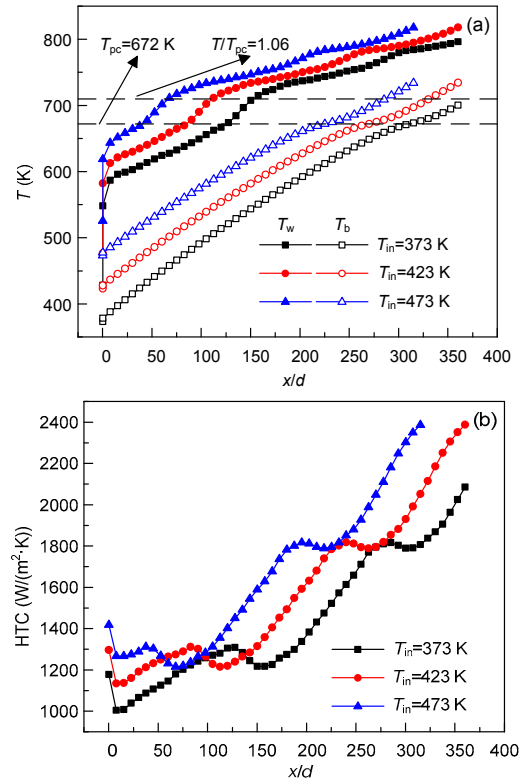


Fig. 10 Distributions of T_w , T_b , and HTC at $m=3.5 \text{ g/s}$, $q_w=200 \text{ kW/m}^2$, and $P=3 \text{ MPa}$ with different T_{in} : (a) variations of T_w and T_b along the tube; (b) variation of HTC along the tube

3.5 Influences of the inlet pressure

As shown in Fig. 1, the fluctuation of thermo-physical properties is much milder with increasing inlet pressure, especially for the specific heat capacity and density. T_{pc} increases from 672 K to 716 K as the pressure rises from 3 MPa up to 5 MPa. As Deterioration I occurs at $T_w=T_{pc}$ under 3 MPa, the change of T_{pc} due to varied inlet pressures will significantly affect the heat transfer performance of the supercritical kerosene.

Fig. 11 shows T_b , T_w , and HTC distributions of the supercritical flow along the axial direction under varied inlet pressures of 3.0, 3.5, 4.0, and 5.0 MPa at $m=3.5 \text{ g/s}$, $q_w=250 \text{ kW/m}^2$, and $T_{in}=423 \text{ K}$. As shown in Fig. 11, T_b increases linearly from the entrance to $x/d=250$, where the divergence takes place and T_b

decreases with increasing P . Similarly, T_w obtained at different P overlaps with each other before $T_w=T_{pc}$. After that, a distinct increase of T_w is observed at $P=3.0$ MPa, while the differences between T_w for other cases are very small. At $x/d=270$, T_w also goes through a similar divergence as that of T_b , where the temperature decreases with decreasing P . Different increase rates of T_w and T_b lead to different heat transfer processes at various P , which are clearly shown in Fig. 11b.

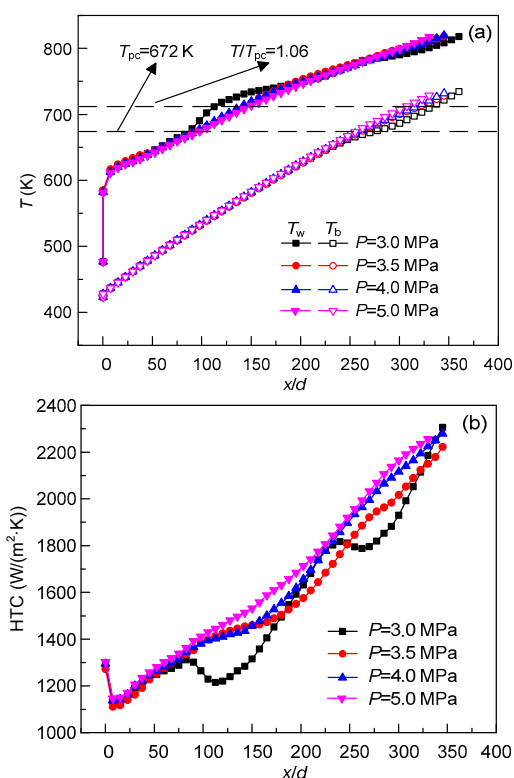


Fig. 11 Distributions of T_w , T_b , and HTC under P ranging from 3 MPa to 5 MPa at $m=3.5$ g/s, $q_w=200$ kW/m², and $T_{in}=423$ K: (a) variations of T_w and T_b along the tube; (b) variation of HTC along the tube

As illustrated in Fig. 11b, the inlet pressure P strongly affects Deterioration I and Deterioration II. The HTC curves at different P deviate from each other after $T_w=T_{pc}$. Though the slope of the heat transfer coefficient decreases with increasing P , Deterioration I and Deterioration II are not observed for the cases with P higher than 3 MPa. As shown in Fig. 1, the changes of kerosene properties become more moderate at $P>3$ MPa, which alleviates the corresponding variation of heat absorption ability and thermal acceleration. As the Reynolds number increases along the tube, the enhancement of turbulence

gradually overcomes the unfavorable deterioration factors, resulting in the disappearances of Deterioration I and Deterioration II.

3.6 Comparisons with empirical heat transfer correlations

Numerical results were compared with three heat transfer correlations proposed by Stigemeier et al. (2002), Li et al. (2011), and Huang et al. (2015a). Huang et al. (2015a) experimentally investigated upward supercritical kerosene with operating conditions of $m=2.0$ – 3.5 g/s, $P=3.6$ – 5.4 MPa, and $q_w=270$ – 350 kW/m². Stigemeier et al. (2002) conducted experiments using five hydrocarbon fuels for the upward flow at $m=12.2$ – 36.7 g/s, $P=6.9$ MPa, and $q_w=321$ – 940 kW/m². Numerical simulation of horizontal kerosene flow was carried out by Li et al. (2011) at $m=56.5$ – 113.1 g/s, $P=4.0$ MPa, and $q_w=300$ – 700 kW/m².

Figs. 12a and 12b show the comparisons of Nu between the numerical data and the values predicted by empirical correlations at $P=3$ MPa and 5 MPa at $m=3.5$ g/s, $q_w=200$ kW/m², and $T_{in}=423$ K. As shown in Fig. 12a, the numerical data fit well with the empirical correlations developed by Stigemeier et al. (2002) and Li et al. (2011) before Deterioration II. However, both these two correlations fail to predict Deterioration I. The Huang et al. (2015a) correlation can predict the occurrence of Deterioration I, but it tends to underestimate our numerical data at $75 \leq x/d \leq 250$. All these three correlations over-predict the numerical data near the outlet of the tube. As listed in Table 1, all these correlations were developed based on $P>3.5$ MPa, under which Deterioration I and Deterioration II were hardly observed. This is a reason for the failure to predict the Deterioration I and Deterioration II using these correlations. For the case of $P=5$ MPa, the numerical data fit well with the Stigemeier et al. (2002) correlation, while the other two tend to underestimate the numerical Nu .

Fig. 12c shows the calculated Nu by empirical correlations against numerical data at $P=3$ – 5 MPa. As shown in Fig. 12c, the calculated Nu fits well with the numerical ones at $Nu_{sim}<100$, after which all these correlations tend to over-predict the numerical data. Most of the calculated Nu falls into the $\pm 30\%$ error bands of the numerical data. The mean absolute deviation (MAD) and the mean relative deviation (MRD) were calculated by

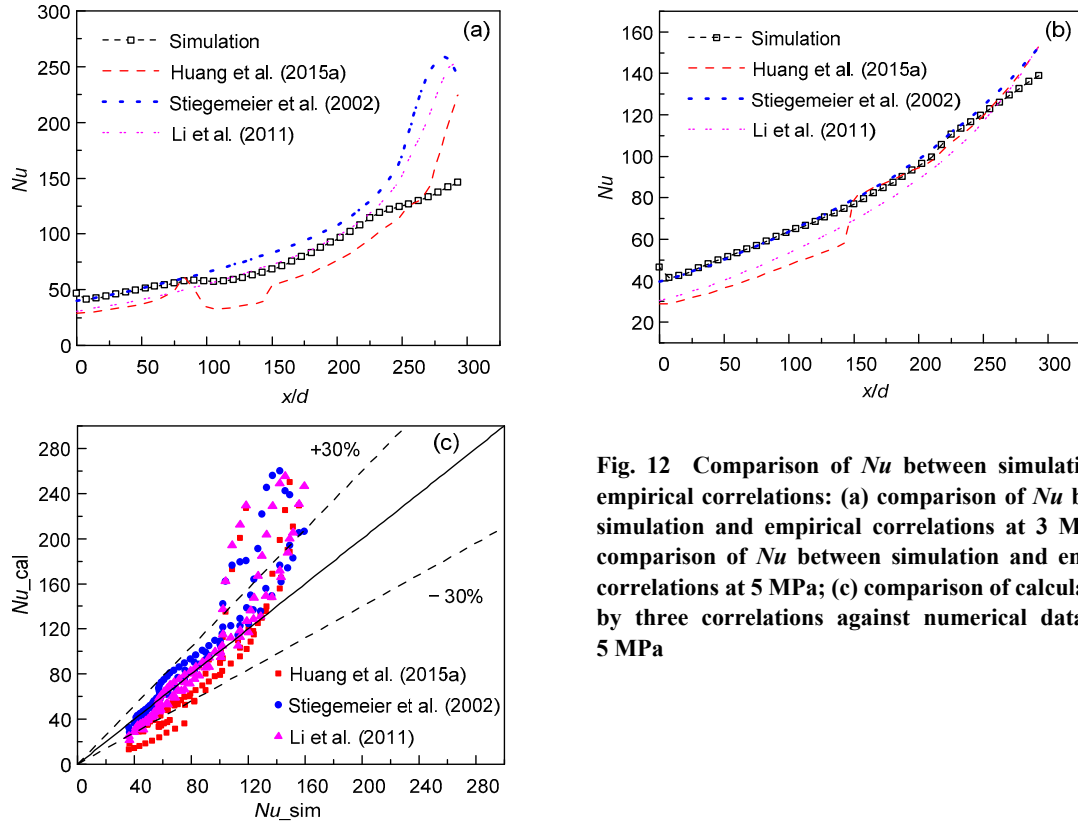


Fig. 12 Comparison of Nu between simulation and empirical correlations: (a) comparison of Nu between simulation and empirical correlations at 3 MPa; (b) comparison of Nu between simulation and empirical correlations at 5 MPa; (c) comparison of calculated Nu by three correlations against numerical data at 3–5 MPa

Table 1 Descriptions of empirical heat transfer correlations

Reference	Correlation	Medium	Pressure (MPa)
Huang et al. (2015a)	$Nu = 0.01019 Re_b^{0.9} Pr_b^{0.42} \left(\frac{c_{p,w}}{c_{p,b}} \right)^{0.87} \left(\frac{\mu_w}{\mu_b} \right)^{0.4137}, \quad T_b / T_c \leq 0.9,$ $Nu = 0.01219 Re_b^{0.92} Pr_b^{0.4} \left(\frac{c_{p,w}}{c_{p,b}} \right)^{0.87} \left(\frac{\mu_w}{\mu_b} \right)^{0.4372}, \quad T_b / T_c > 0.9$	China RP-3 aviation kerosene	3.6–5.4
Stiegemeier et al. (2002)	$Nu = 0.016 \left(1 + \frac{2}{x/d} \right) Re_b^{0.862} Pr_b^{0.4}$	JP-7, JP-8, JP-8+100, JP-10, and RP-1	6.9
Li et al. (2011)	$Nu = 0.0435 Re_b^{0.8}$	China RP-3 aviation kerosene	4.0

Note: Nu is the Nusselt number; Re is the Reynolds number; Pr is the Prandtl number; d is the tube diameter (m); the subscripts b, w, and c represent the fluid bulk, the tube wall, and the critical point, respectively

$$MAD = \frac{1}{N} \sum_{i=1}^N \left| \frac{U_{pre} - U_{sim}}{U_{sim}} \right| \times 100\%, \quad (10)$$

$$MRD = \frac{1}{N} \sum_{i=1}^N \frac{U_{pre} - U_{sim}}{U_{sim}} \times 100\%, \quad (11)$$

where U_{pre} and U_{sim} are the predictive value and the numerical value, respectively, and N is the number of data.

Table 2 lists the MAD and MRD of the three heat transfer correlations under different pressures. It is indicated that all the aforementioned correlations show better predictions for the cases at 5 MPa compared with those at 3 MPa. The correlation proposed by Li et al. (2011) fits best with the numerical results under 3 MPa, while the correlation proposed by Stiegemeier et al. (2002) exhibits better performance under 5 MPa compared with the others. Overall, the

Table 2 MAD and MRD of empirical heat transfer correlations under different pressures

Criterion	MAD			MRD		
	$P=3$ MPa	$P=5$ MPa	Overall	$P=3$ MPa	$P=5$ MPa	Overall
Huang et al. (2015a)	24.31%	15.05%	28.26%	-17.87%	-12.84%	-14.17%
Stiegemeier et al. (2002)	21.89%	2.86%	16.33%	21.21%	1.62%	14.38%
Li et al. (2011)	17.44%	12.58%	20.20%	4.88%	-11.37%	3.07%

correlation proposed by Stiegemeier et al. (2002) can predict our numerical simulation best compared with the other two.

4 Conclusions

In the present work, the convective heat transfer characteristics of the downward RP-3 aviation kerosene under supercritical pressure in circular tubes were studied numerically using the RNG k - ϵ two-equation turbulent model. The effects of mass flow rate (3.0–5.0 g/s), wall heat flux (150–300 kW/m²), inlet pressure (3–5 MPa), and temperature (373–473 K) on the HTC were investigated. Those effects on the heat transfer characteristics of supercritical RP-3 aviation kerosene were studied by the variation of one parameter at a time. Three types of heat transfer deteriorations in the downward flow were discussed. Based on the numerical results, several conclusions can be obtained in the present work as follows:

1. Three types of heat transfer deteriorations were observed in the downward supercritical flow. The first type of deterioration is caused by the development of the thermal boundary layer and exists at the entrance of the tube within $x/d=10$. The second and third types of deterioration appear when the wall or bulk fuel temperature approaches the pseudo-critical temperature. Drastic variations of the kerosene properties and the concurrent thermal acceleration effect in the near-wall region are the main reasons for the second type of deterioration. The insufficient cooling of the heated wall resulting from the unusual radial velocity distribution leads to the occurrence of the third type of deterioration.

2. The HTC increases with increasing mass flow rate at the same bulk fuel temperature. The mass flow rate has no effect on the end of Deterioration near the inlet, while a higher mass flow rate delays the onsets

of Deterioration I and Deterioration II. The relative degree of Deterioration II is severer as the mass flow rate increases.

3. The effect of q_w on the thermal boundary layer is more intense under a higher heat flux. The onsets of Deterioration I and Deterioration II are delayed along the tube axial direction under lower q_w , while the deterioration is more pronounced at a higher wall heat flux.

4. The inlet temperature only affects the starting point of the heat transfer process at fixed m , P , and q_w , while it has little effect on the heat transfer coefficient. The effect of P on Deterioration near the inlet is negligible, while it strongly affects Deterioration I and Deterioration II. Deterioration I and Deterioration II are not observed for the cases with P higher than 3 MPa because of the more moderate variations of properties of kerosene under higher pressures.

5. The numerical data fit well with the empirical correlations proposed by Stiegemeier et al. (2002), Li et al. (2011), and Huang et al. (2015a) under a pressure of 3–5 MPa. Most of the calculated Nu falls into the $\pm 30\%$ error bands of the numerical data. The Stiegemeier et al. (2002) correlation can predict the heat transfer coefficient best with the MAD and MRD of 16.33% and 14.38%, respectively. Note that the MAD and MRD are limited to the computed cases in the present work, and more studies are needed to evaluate the prediction of aforementioned empirical correlations.

References

- ANSYS, 2013. ANSYS FLUENT User's Guide, Release 15.0. ANSYS, Inc, USA.
- Bae YY, Kim HY, 2009. Convective heat transfer to CO₂ at a supercritical pressure flowing vertically upward in tubes and an annular channel. *Experimental Thermal and Fluid Science*, 33(2):329-339. <https://doi.org/10.1016/j.expthermflusci.2008.10.002>
- Dang G, Zhong F, Chen L, et al., 2013. Numerical investigation on flow and convective heat transfer of aviation kerosene at supercritical conditions. *Science China Technological*

- Sciences*, 56(2):416-422.
<https://doi.org/10.1007/s11431-012-5075-3>
- Dang G, Zhong F, Zhang Y, et al., 2015. Numerical study of heat transfer deterioration of turbulent supercritical kerosene flow in heated circular tube. *International Journal of Heat and Mass Transfer*, 85(0):1003-1011.
<https://doi.org/10.1016/j.ijheatmasstransfer.2015.02.052>
- Deng H, Zhu K, Xu G, et al., 2012. Heat transfer characteristics of RP-3 kerosene at supercritical pressure in a vertical circular tube. *Journal of Enhanced Heat Transfer*, 19(5):409-421.
<https://doi.org/10.1615/JEnhHeatTransf.2012004966>
- Edwards T, 2003. Liquid fuels and propellants for aerospace propulsion: 1903–2003. *Journal of Propulsion and Power*, 19(6):1089-1107.
<https://doi.org/10.2514/2.6946>
- Huang D, Ruan B, Wu X, et al., 2015a. Experimental study on heat transfer of aviation kerosene in a vertical upward tube at supercritical pressures. *Chinese Journal of Chemical Engineering*, 23(2):425-434.
<https://doi.org/10.1016/j.cjche.2014.10.016>
- Huang D, Wu X, Wu Z, et al., 2015b. Experimental study on heat transfer of nanofluids in a vertical tube at supercritical pressures. *International Communications in Heat and Mass Transfer*, 63:54-61.
<https://doi.org/10.1016/j.icheatmasstransfer.2015.02.007>
- Jiang PX, Liu B, Zhao CR, et al., 2013. Convection heat transfer of supercritical pressure carbon dioxide in a vertical micro tube from transition to turbulent flow regime. *International Journal of Heat and Mass Transfer*, 56(1-2):741-749.
<https://doi.org/10.1016/j.ijheatmasstransfer.2012.08.038>
- Li W, Huang D, Xu GQ, et al., 2015. Heat transfer to aviation kerosene flowing upward in smooth tubes at supercritical pressures. *International Journal of Heat and Mass Transfer*, 85:1084-1094.
<https://doi.org/10.1016/j.ijheatmasstransfer.2015.01.079>
- Li X, Zhong F, Fan X, et al., 2010. Study of turbulent heat transfer of aviation kerosene flows in a curved pipe at supercritical pressure. *Applied Thermal Engineering*, 30(13):1845-1851.
<https://doi.org/10.1016/j.applthermaleng.2010.04.022>
- Li X, Huai X, Cai J, et al., 2011. Convective heat transfer characteristics of China RP-3 aviation kerosene at supercritical pressure. *Applied Thermal Engineering*, 31(14-15):2360-2366.
<https://doi.org/10.1016/j.applthermaleng.2011.03.036>
- Li Z, Wu Y, Tang G, et al., 2015. Comparison between heat transfer to supercritical water in a smooth tube and in an internally ribbed tube. *International Journal of Heat and Mass Transfer*, 84:529-541.
<https://doi.org/10.1016/j.ijheatmasstransfer.2015.01.047>
- Pizzarelli M, Urbano A, Nasuti F, 2010. Numerical analysis of deterioration in heat transfer to near-critical rocket propellants. *Numerical Heat Transfer, Part A: Applications*, 57(5):297-314.
<https://doi.org/10.1080/10407780903583016>
- Stigemeier B, Meyer M, Taghavi R, 2002. A thermal stability and heat transfer investigation of five hydrocarbon fuels: JP-7, JP-8, JP-8+100, JP-10, and RP-1. 38th AIAA/ASME/SAE/ASEE Joint Propulsion Conference & Exhibit, No. AIAA 2002-3873.
- Urbano A, Nasuti F, 2013. Conditions for the occurrence of heat transfer deterioration in light hydrocarbons flows. *International Journal of Heat and Mass Transfer*, 65: 599-609.
<https://doi.org/10.1016/j.ijheatmasstransfer.2013.06.038>
- Wang J, Li H, Yu S, et al., 2011. Investigation on the characteristics and mechanisms of unusual heat transfer of supercritical pressure water in vertically-upward tubes. *International Journal of Heat and Mass Transfer*, 54(9-10):1950-1958.
<https://doi.org/10.1016/j.ijheatmasstransfer.2011.01.008>
- Wang K, Xu X, Wu Y, et al., 2015. Numerical investigation on heat transfer of supercritical CO₂ in heated helically coiled tubes. *The Journal of Supercritical Fluids*, 99: 112-120.
<https://doi.org/10.1016/j.supflu.2015.02.001>
- Wang YZ, Hua YX, Meng H, 2010. Numerical studies of supercritical turbulent convective heat transfer of cryogenic-propellant methane. *Journal of Thermophysics and Heat Transfer*, 24(3):490-500.
<https://doi.org/10.2514/1.46769>
- Xu K, Meng H, 2015a. Analyses of surrogate models for calculating thermophysical properties of aviation kerosene RP-3 at supercritical pressures. *Science China Technological Sciences*, 58(3):510-518.
<https://doi.org/10.1007/s11431-014-5752-5>
- Xu K, Meng H, 2015b. Modeling and simulation of supercritical-pressure turbulent heat transfer of aviation kerosene with detailed pyrolytic chemical reactions. *Energy & Fuels*, 29(7):4137-4149.
<https://doi.org/10.1021/acs.energyfuels.5b00097>
- Yang C, Xu J, Wang X, et al., 2013. Mixed convective flow and heat transfer of supercritical CO₂ in circular tubes at various inclination angles. *International Journal of Heat and Mass Transfer*, 64:212-223.
<https://doi.org/10.1016/j.ijheatmasstransfer.2013.04.033>
- Zhang C, Xu G, Gao L, et al., 2012. Experimental investigation on heat transfer of a specific fuel (RP-3) flows through downward tubes at supercritical pressure. *The Journal of Supercritical Fluids*, 72:90-99.
<https://doi.org/10.1016/j.supflu.2012.07.011>
- Zhang C, Xu G, Deng H, et al., 2013. Investigation of flow resistance characteristics of endothermic hydrocarbon fuel under supercritical pressures. *Propulsion and Power Research*, 2(2):119-130.
<https://doi.org/10.1016/j.jprr.2013.04.002>
- Zhong F, Fan X, Yu G, et al., 2009a. Heat transfer of aviation kerosene at supercritical conditions. *Journal of Thermophysics and Heat Transfer*, 23(3):543-550.
<https://doi.org/10.2514/1.41619>

Zhong F, Fan X, Yu G, et al., 2009b. Thermal cracking of aviation kerosene for scramjet applications. *Science in China Series E: Technological Sciences*, 52(9):2644-2652.

<https://doi.org/10.1007/s11431-009-0090-8>

Zhong F, Fan X, Yu G, et al., 2011. Thermal cracking and heat sink capacity of aviation kerosene under supercritical conditions. *Journal of Thermophysics and Heat Transfer*, 25(3):450-456.

<https://doi.org/10.2514/1.51399>

中文概要

题目: 圆管内向下流超临界航空煤油换热特性数值研究
目的: 超临界航空煤油在换热过程中会出现传热恶化的

现象。本文旨在研究该现象产生的原因及质量流量、壁面热流、入口温度和压力对此现象的影响。

创新点: 1. 分析超临界航空煤油的传热恶化现象；2. 揭示超临界航空煤油传热过程中传热恶化现象与质量流量、壁面热流、入口温度及压力的关系。

方法: 利用数值模拟的方法，模拟超临界航空煤油在管内的流动换热情况，分析其换热特性，并探讨传热恶化产生的原因及影响因素。

结论: 1. 传热恶化是在壁面温度达到拟临界温度或流体平均温度达到临界温度时产生的；2. 换热系数随质量流量的增加或壁面热流的降低而增大；3. 通过提高煤油的压力可以显著降低恶化现象。

关键词: 航空煤油；传热恶化；超临界；数值研究